01 Dec 2016

High Order Harmonic Generation from SF_6: Deconvolution of Macroscopic Effects

B. P. Wilson

K. D. Fulfer

S. Mondal

X. Ren

et. al. For a complete list of authors, see https://scholarsmine.mst.edu/phys_facwork/1632

Recommended Citation

B. P. Wilson and K. D. Fulfer and S. Mondal and X. Ren and J. Tross and E. D. Poliakoff and J. Jose and A. Le and R. R. Lucchese and C. A. Trallero-Herrero, "High Order Harmonic Generation from SF_6: Deconvolution of Macroscopic Effects," *Journal of Chemical Physics*, vol. 145, no. 22, American Institute of Physics (AIP), Dec 2016.
The definitive version is available at https://doi.org/10.1063/1.4971244

High order harmonic generation from SF_6: Deconvolution of macroscopic effects

B. P. Wilson,[1] K. D. Fulfer,[1] S. Mondal,[2] X. Ren,[2] J. Tross,[2] E. D. Poliakoff,[1] J. Jose,[3,4] Anh-Thu Le,[2] R. R. Lucchese,[3] and C. Trallero-Herrero[2]
[1]*Department of Chemistry, Louisiana State University, Baton Rouge, Louisiana 70803, USA*
[2]*J.R. Macdonald Laboratory, Kansas State University, Manhattan, Kansas 66506, USA*
[3]*Department of Chemistry, Texas A&M University, College Station, Texas 77843, USA*
[4]*Department of Physics, Indian Institute of Technology Patna, Bihta 801103, India*

(Received 1 July 2016; accepted 17 November 2016; published online 13 December 2016)

We measure high order harmonics from the molecule SF_6 over a large range of phase matching conditions and observe several features in the harmonics that are largely independent of such macroscopic conditions. The experimental data are then compared to the quantitative rescattering theory for the generation of harmonics from three orbitals. With this comparison, we are able to assign spectroscopic features in the harmonics to contributions from $1t_{1g}$ (HOMO) and $5t_{1u}$ (HOMO-1) orbitals. *Published by AIP Publishing.* [http://dx.doi.org/10.1063/1.4971244]

I. INTRODUCTION

High order harmonic generation (HHG)[1,2] is a source of coherent, high energy radiation that has been studied extensively for its potential as an X-ray and XUV table top source[3] and as the main mechanism for the generation of attosecond pulses.[4–6] In a semiclassical approximation, HHG is usually described by the following three step process: first, an atom or molecule undergoes tunnel ionization which frees an electron wave packet; second, the wave packet is accelerated away from the ion and driven back by the laser pulse; third, recollision of the electron wave packet with the parent ion and photorecombination results in the release of a high energy photon.[1,2] Recently, a quantitative rescattering (QRS) theory for molecules has been developed that has demonstrated that the harmonic signal is approximately the product of the electron wave packet intensity and the photorecombination cross section.[7,8] Since the photorecombination step is related to photoionization by time reversal, in the QRS model the energy dependent spectroscopic features observed in the corresponding photoionization cross sections are also present in the harmonic signal.[9–11] While the extraction of the photorecombination matrix elements has already been attempted,[11,12] two primary complications inherent in HHG prevent this direct extraction. First, the harmonic envelope can be changed dramatically depending on the macroscopic conditions.[13–15] Second, it is possible for electrons from more than a single orbital to participate in the HHG process, particularly from molecules which are typically characterized by relatively closely spaced outermost orbitals.[16]

In this paper, we perform a combined experimental and theoretical study of HHG from SF_6, with the goal of understanding how molecular scattering effects are manifested in the HHG spectra of complex molecules. Previous studies have shown the influence of several dynamical processes in HHG spectra,[10,12,17–21] we extend the investigation of the relationship between the photoionization cross section with the photorecombination cross section by studying harmonic generation from SF_6, a molecule with intense shape resonances and whose photoionization dynamics have been investigated extensively.[22–29] Shape resonances are ubiquitous in molecular systems and manifest themselves as an enhancement in the photoelectron yield. We note that resonant enhancements have been observed in HHG from atoms[12] and the effects of shape resonances have been seen in HHG from molecular systems, e.g., for N_2 [11,30] and more recently SF_6.[31,32] The study by Ferré *et al.*[31] on the HHG of SF_6 confirms the presence of a shape resonance in the HHG spectrum between the harmonics 13th (H13) and 17th (H17) of the 800 nm driving pulse corresponding to energies of 20 eV and 26 eV, respectively. In the paper by Manschwetus *et al.*,[32] the minimum in the HHG at H17 is also observed and evidence is given that indicates that there are contributions from multiple active electron channels. In the present paper, we examine the effects of shape resonances over a broad range of the HHG spectrum in SF_6 and we also consider the influence of macroscopic propagation effects and the effects of photorecombination dynamics from multiple molecular orbitals.

Studying the broad HHG spectrum for shape resonant effects and assigning these features requires a theoretical foundation. To assign the observed features in the harmonic spectra to molecular structure, we performed theoretical calculations simulating the HHG process in SF_6. We have considered HHG generation from the $1t_{1g}$ (HOMO), $5t_{1u}$ (HOMO-1), and $1t_{2u}$ (HOMO-2) orbitals, which have ionization potentials (IPs) within 1.5 eV of each other. As mentioned above, these calculations are done using the QRS framework which is based on the three-step model for HHG.[2] The QRS method[7] is a variant of the strong-field approximation (SFA) and has proven to be an excellent tool for analyzing HHG from atoms and molecules.[7,8,11,21] We analyze the relative strength and phase of the harmonic emission from multiple valence orbitals in order to identify the contributing dynamics in the experimental harmonic spectrum.

Additionally, for HHG generated from an isotropic distribution of target orientations, we consider the importance of making a coherent orientation average in modeling the generated HHG.

II. EXPERIMENTAL

The experimental setup is sketched schematically in Fig. 1. The fundamental IR pulses were provided by the J.R. Macdonald's lab HITS laser described in Ref. 33. In short, the laser is a multi-pass, two stage amplified ultrafast laser capable of 20 mJ of energy per pulse with 25 fs FWHM of the intensity pulse duration and a center wavelength of 800 nm (1.55 eV) at 1 kHz repetition rate. The pulse energy is first reduced with a series of beam splitters and then finely controlled with an automated half-wave plate directly in front of a linear polarizer, in order to maintain a constant focal condition. The beam is then focused onto the gas jet by a plano-convex lens with a 1 m focal length to a maximum peak intensity of ca. 5.2×10^{14} W/cm^2.

Our CW gas jet is provided by a glass nozzle with an aperture of ca. 0.15 mm. The backing pressure behind the nozzle is held near 100 Torr with a needle valve used to maintain a source chamber pressure of approximately 10^{-5} Torr. The position of the lens is adjusted using an automated linear stage. The distance of the focal point from the center of the gas jet is described as being (−) when the focus is in front of the gas jet and (+) when the focal point is behind the gas jet. The specific distance on either side of the gas jet was determined by monitoring the ion signal with a channeltron while the harmonic spectra were taken. The ion intensity was fitted as a function of lens position to a Gaussian distribution, with the center of the gas jet defined by the peak ion intensity. Because the ion signal is only dependent on gas density and peak intensity, it provides an unambiguous reference for the focus position relative to the gas jet.

The resulting beam is a mixture of the harmonics and principle beams which are separated by a Shimadzu 30-002 soft x-ray flat-field diffraction grating with a groove density of 1200 grooves/mm positioned after a 0.1 mm slit. The harmonics are collimated onto a position sensitive detector consisting of a set of microchannel plates in the "z-stack" configuration and phosphor screen. A Hamamatsu Orca-flash complementary metal-oxide semiconductor (CMOS) camera then monitors the phosphor screen and records images, such as the inset in Fig. 1. A background image was taken for each laser intensity with the gas jet off and was then subtracted from each image with the gas jet on.

From the resulting images, the harmonic intensities were obtained by integrating over the vertical pixels to create the harmonic lineouts. The lineouts were normalized to the total harmonic sum. The peak intensities for each harmonic are then presented as the harmonic envelope in the remainder of this paper. The above procedure was repeated ten times for every focal position and intensity combination and the average of these replicates is presented here, with the standard deviation presented as error bars.

III. THEORETICAL METHODOLOGY

Here we model the HHG spectrum using QRS[7,8] theory. In this model, the HHG power spectrum, S, at frequency ω for linearly polarized excitation laser with the polarization in the (θ, ϕ) direction in the molecular frame is given by (in atomic units)[34]

$$S(\omega, \theta, \phi) = \frac{2\omega^4}{3\pi c^3} |D(\omega, \theta, \phi)|^2, \quad (1)$$

where $D(\omega, \theta, \phi)$ is the complex-valued induced dipole. In the QRS, the contribution of each ionization channel to $D(\omega, \theta, \phi)$ is written as the product of the wave packet $W_i(E, \theta, \phi)$ of the returning electron, with energy $E_i = \omega - I_i$ where I_i is the IP of the target molecule for ionization from state ψ_i, and the photorecombination transition dipole $d_i(\omega, \theta, \phi)$

$$D(\omega, \theta, \phi) = \sum_i W_i(E_i, \theta, \phi)\, d_i(\omega, \theta, \phi). \quad (2)$$

The most general photorecombination matrix has the form $d_i(\omega, \theta, \phi, \theta_k, \phi_k)$ where (θ, ϕ) is the direction of the transition dipole and (θ_k, ϕ_k) is the asymptotic direction of the incoming recaptured electron. The photorecombination matrix elements can be obtained from the corresponding photoionization matrix elements by time reversal, i.e., taking the complex conjugate and inverting the direction of the photoelectron momentum. In the QRS model of the HHG process with linearly polarized light, the polarization direction and the photoelectron direction are taken to be the same so that we use the symbol $d_i(\omega, \theta, \phi)$ to indicate the transition dipole where both the field and the motion of the active electron are in the (θ, ϕ) direction.

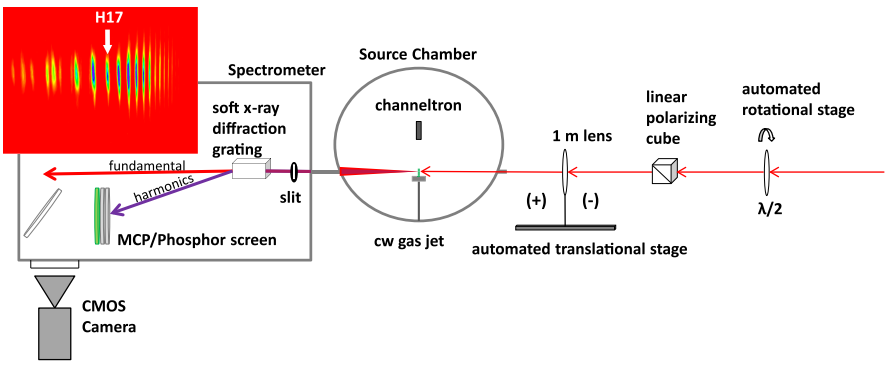

FIG. 1. Block diagram of the experimental apparatus with a sample HHG image in the inset. The photon energy in the inset increases from left to right.

In QRS2,[7,8] which is used here, the wave packet $W_i(E,\theta,\phi)$ is approximated by

$$W_i(E_i,\theta,\phi) = \left[\frac{N_i(\theta,\phi)}{N_i^{\rm ref}}\right]^{\frac{1}{2}} \frac{D_i^{\rm ref}(\omega)}{d_i^{\rm ref}(\omega)} e^{i\Delta\eta_i(E_i,\theta,\phi)}, \tag{3}$$

where $N_i(\theta,\phi)$ and $N_i^{\rm ref}$ are the ionization probabilities for electron emission in the direction of polarization of the laser from the orbital ψ_i of the molecule and a scaled H(1s) reference atom with the same I_i, respectively, which are calculated using the molecular SFA (MO-SFA) theory.[7,35] $\Delta\eta_i(E_i,\theta,\phi)$is introduced to account for the phase difference between the two wave packets, which is approximated by the energy-independent phase of the asymptotic wave function of the active electron.[8] $d_i^{\rm ref}(\omega)$ is the transition dipole for the reference atom from the well-known exact analytical expression for scaled H(1s). One can calculate $D_i^{\rm ref}$ for the reference atom by numerically solving the time-dependent Schrödinger equation (TDSE), which is time consuming. Alternatively, in the present study the SFA method[35] is used to calculate $D^{\rm ref}$. The wave packet can be written as

$$W_i(E_i,\theta,\phi) = X_i^{\rm ref}(\omega)\left[N_i(\theta,\phi)\right]^{\frac{1}{2}} e^{i\Delta\eta_i(E_i,\theta,\phi)}, \tag{4}$$

where $X_i^{\rm ref}(\omega)$ is independent of the direction of the light polarization and depends only on the exciting field and the reference atom, and is given by

$$X_i^{\rm ref}(\omega) = \frac{D_i^{\rm ref}(\omega)}{\left(N_i^{\rm ref}\right)^{\frac{1}{2}} d_i^{\rm ref}(\omega)}. \tag{5}$$

In the present study we have not considered aligned molecular targets and thus we have averaged the induced dipole over all possible orientations of the target molecules in the field. Equivalently for linearly polarized light, we can average the field direction over all directions in the molecular frame giving[8]

$$\overline{D}(\omega) = \frac{1}{4\pi}\int_0^{\pi} d\theta \int_0^{2\pi} d\phi \sin\theta\, D(\omega,\theta,\phi). \tag{6}$$

The final expression for the power spectrum is then[8]

$$S(\omega) = \frac{2\omega^4}{3\pi c^3}\left|\sum_i g_i X_i^{\rm ref}(\omega)\frac{1}{4\pi}\int_0^{\pi} d\theta \int_0^{2\pi} d\phi \sin\theta \left[N_i(\theta,\phi)\right]^{\frac{1}{2}} e^{i\Delta\eta_i(E_i,\theta,\phi)} d_i(\omega,\theta,\phi)\right|^2, \tag{7}$$

where g_i is the degeneracy of the active orbital ψ_i. Note that for tunneling from degenerate orbitals, as is the case considered here, when the degenerate set of orbitals can be rotated into each other, the total rate is just the rate from one of the orbitals multiplied by the degeneracy of the orbitals[36] as indicated in Eq. (7).

As written, Eq. (7) includes a fully coherent sum over the contributions from the ion channels and a coherent orientation average. The validity of this form is based on the assumption that the relative phase between the induced dipoles from the different orbitals is adequately captured by the relative phase of the induced dipoles from the reference atom, $D_i^{\rm ref}(\omega)$. To explore the size of this possible inter-channel phase effect, we also give results based on Eq. (7) but using an incoherent sum over channels, with the form

$$S'(\omega) = \frac{2\omega^4}{3\pi c^3}\sum_i g_i^2 \left|X_i^{\rm ref}(\omega)\right|^2 \left|\frac{1}{4\pi}\int_0^{\pi} d\theta \int_0^{2\pi} d\phi \sin\theta \left[N_i(\theta,\phi)\right]^{\frac{1}{2}} e^{i\Delta\eta_i(E_i,\theta,\phi)} d_i(\omega,\theta,\phi)\right|^2. \tag{8}$$

Furthermore, when only the total photoionization cross section is known and not the dipole matrix elements, one can approximate Eq. (8) to yield an expression for the power spectrum of the form

$$S''(\omega) = \sum_i \frac{2\omega^4\left|X_i^{\rm ref}(\omega)\right|^2}{3\pi c^3}\overline{N}_i\frac{\sigma_i(\omega)}{4\pi}\frac{c}{4\pi^2\omega}, \tag{9}$$

where the average molecular tunneling rate is

$$\overline{N}_i = \frac{1}{4\pi}\int_0^{\pi} d\theta \int_0^{2\pi} d\phi \sin\theta\, N_i(\theta,\phi) \tag{10}$$

and $\sigma_i(\omega)$ is the total photoionization cross section for ionization from orbital i, given by the incoherent orientation average

$$\sigma_i(\omega) = \frac{4\pi^2\omega}{c}\frac{1}{4\pi}\int_0^{\pi} d\theta \int_0^{2\pi} d\phi \sin\theta \int_0^{\pi} d\theta_k \int_0^{2\pi} d\phi_k \sin\theta_k \left|d_i(\omega,\theta,\phi,\theta_k,\phi_k)\right|^2, \tag{11}$$

where the absolute square of the photoionization dipole matrix $d_i(\omega, \theta, \phi, \theta_k, \phi_k)$ has been averaged over all polarization directions (θ, ϕ) and integrated over all photoelectron emission directions (θ_k, ϕ_k). To the extent that Eq. (9) is valid, a measured HHG yield could be used to determine the total photoionization cross section.[8,37,38] This incoherent orientation average is also the approximation of the power spectrum implicitly used to analyze the HHG spectrum in an earlier study of SF_6.[31]

An alternative to obtaining $X_i^{\text{ref}}(\omega)$ from a calculation on a model atom is to use a measured HHG spectrum, $S_i^{\text{ref}}(\omega)$, of a reference atom with the same ionization potential as the molecular orbital ψ_i obtained under the same experimental conditions as for the molecule under study. In that case, using independently measured cross sections, $\sigma_i^{\text{ref}}(\omega)$, and photoelectron asymmetry parameters, $\beta_i^{\text{ref}}(\omega)$, the part of the wave packet from the reference atom can be estimated by

$$\left|X_i^{\text{ref}}(\omega)\right|^2 = \frac{24\pi^4 c^2}{\omega^3} \frac{S_i^{\text{ref}}(\omega)}{N_i^{\text{ref}} \sigma_i^{\text{ref}}(\omega) \left[1 + \beta_i^{\text{ref}}(\omega)\right]}, \quad (12)$$

where the tunneling rate N_i^{ref} is an overall factor that is independent of the energy and is thus not needed to determine the relative values of the returning wave packet.

The dipole photorecombination parameters were obtained using two different methods. The first method used the frozen-core Hartree-Fock (FCHF) approximation[39] as evaluated in the ePolyScat code.[28,40] In these calculations, the initial and final bound molecular electronic states were constructed from single configuration state functions (CSFs) using the Hartree-Fock orbitals of the neutral molecule. The photoionization calculations were then performed in the uncoupled single-channel approximation. For the second method, we performed multichannel frozen-core Hartree-Fock (MCFCHF) calculations[41] using the complex Kohn method.[42,43] In MCFCHF calculations, the target states were the same as in the FCHF case; however, the different ionization channels were coupled together in a close-coupling expansion. These photoionization calculations are very similar to those published earlier.[44] All calculations were performed using the fixed-nuclei approximation, thus not allowing for the treatment of nuclear motion during the HHG process.

IV. RESULTS

A. Experimental results

The strong field in HHG, necessary for tunnel ionization, influences the macroscopic propagation effects in the generating medium. Of particular interest is the location of the focal point with respect to the medium, which can determine which quantum trajectory is favored.[14,45–47] The nature of the electron trajectory before recollision is of importance because it determines the time scale of the emitted harmonics.[48] We distinguish between long and short trajectories by their appearance in the raw images taken following the criteria proposed by Bellini *et al.*[49] Briefly, the center annular part of the harmonics is assumed to be the on-axis contribution from the short trajectories, while the spatially distorted portions of the photon beams are from off-axis contributions, attributed to long trajectories. In the case of SF_6, for this particular laser, we observe purely short trajectories at all lens positions. Since our gas jet is much smaller than the Rayleigh range of the focused laser beam, we are in the soft focusing regime where phase matching enhances short trajectories. However, our observations of short-trajectories are valid for this particular laser and high ionization potential molecules. In general phase-matching is very laser-mode dependent and these observations cannot be generalized.

In the following paragraphs, in order to make the comparison with the theoretical results more clear, we will refer to the harmonics by their photon energy.

Figure 2 shows HHG spectra for SF_6 at different focal point positions with a constant peak intensity of 4.0×10^{14} W/cm^2. There are three salient features: maxima at 23 eV (H15) and 33 eV (H21) harmonics, and a minimum at 26 eV (H17). The minimum at 26 eV in the SF_6 data is present in every combination of laser intensity and lens position, while the maximum at 33 eV (H21) is more prominent in the (−) positions. The consistency of the position in the harmonics

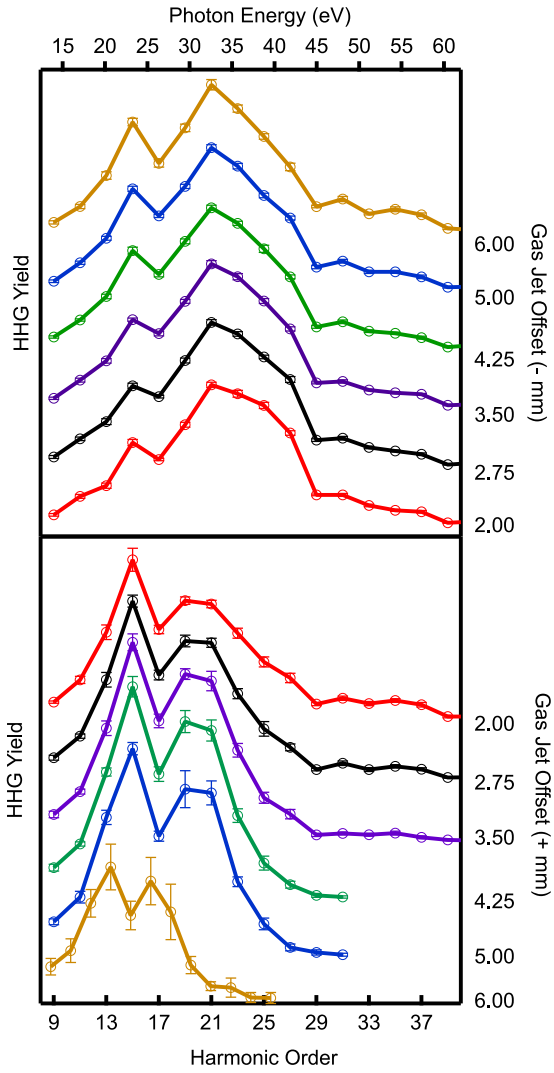

FIG. 2. Position dependence of the measured SF_6 harmonic spectrum at 4.0×10^{14} W/cm^2. The (−) positions indicate a situation where the focal point is in front of the center of the gas jet.

spectra of dynamical effects with respect to changes in the position of the focal point is in contrast with previous studies. For example, a change in the position of the Cooper minimum in Ar as the lens position is changed has previously been identified.[10,19,50] In addition to SF_6, we also took harmonic spectra of Ar, as mentioned below, but see no evidence of the Cooper minimum shifting with macroscopic phase matching conditions. Because many of the features we observe persist over a broad range of phase matching conditions, we conclude that the experimental HHG spectra can be understood in terms of a single molecule response such as in the QRS.

Harmonic spectra for SF_6 are shown in Fig. 3 as a function of intensity. In the figure, we plot harmonic spectra for intensities ranging from 1.7×10^{14} W/cm^2 to 4.8×10^{14} W/cm^2 with the focal point located 2.75 mm before and after the center of the gas jet. The overall spectral lineout, the peak centered at 23 eV (H15), and the minimum centered at 26 eV (H17) do not change with peak laser intensity at any lens position which strongly suggests that the features in the low energy range of the spectrum are the result of an interaction in the photorecombination step. The enhancement at 33 eV (H21) in SF_6 is also stable with respect to changes in intensity, maintaining the intensity of the peak even as the laser intensity is significantly reduced. It should be noted that while the enhancements in the upper panel of Fig. 3 are maintained at all intensities, the minimum at 26 eV (H17) becomes less pronounced as the intensity is increased.

The corresponding spectra for HHG in Ar with the laser focus at (−) 2.75 mm and varying power are give in Fig. 4. One can see the evidence of the Cooper minimum near 50 eV. The yield curve with laser intensity of 2.5×10^{14} W/cm^2 will be used to construct a reference atom wave packet using Eq. (12) above.

B. Theoretical results

In order to clarify the shape resonant effects observed in our experimental data, the HHG spectrum is investigated using QRS theory. The one-photon ionization dynamics of SF_6 have been studied extensively.[22–29,44,51] The photoionization from valence orbitals with even parity has well-known shape resonances[25,29,44,52] with t_{1u} symmetry about 2 eV above threshold and t_{2u} symmetry at about 20 eV above threshold, while the orbitals with odd parity have commonly accessed shape resonances of t_{2g} symmetry about 7 eV above threshold and e_g symmetry at about 20 eV above threshold. In the QRS and scattering calculations, we used the experimental IPs[25] that are $I_i\left(1t_{1g}\right) = 15.7$ eV for the IP of the HOMO, $I_i\left(5t_{1u}\right) = 16.9$ eV for the HOMO-1, and $I_i\left(1t_{2u}\right) = 17.2$ eV for the HOMO-2. The ground state of the SF_6 was represented by the Hartree-Fock wave function that was computed using the Gaussian[53] quantum chemistry code with a 6-311+G(2d) basis set using a bond length of R(S-F) = 1.561 Å.[54] The photoionization in the single-channel FCHF approximation was computed using the single-center-expansion scattering code ePolyScat[28,40] using a maximum partial-wave expansion of $l_{max} = 120$ and the full O_h symmetry in the wave functions. The coupled-channel photoionization calculations were performed using the complex Kohn scattering codes.[42,43] In these

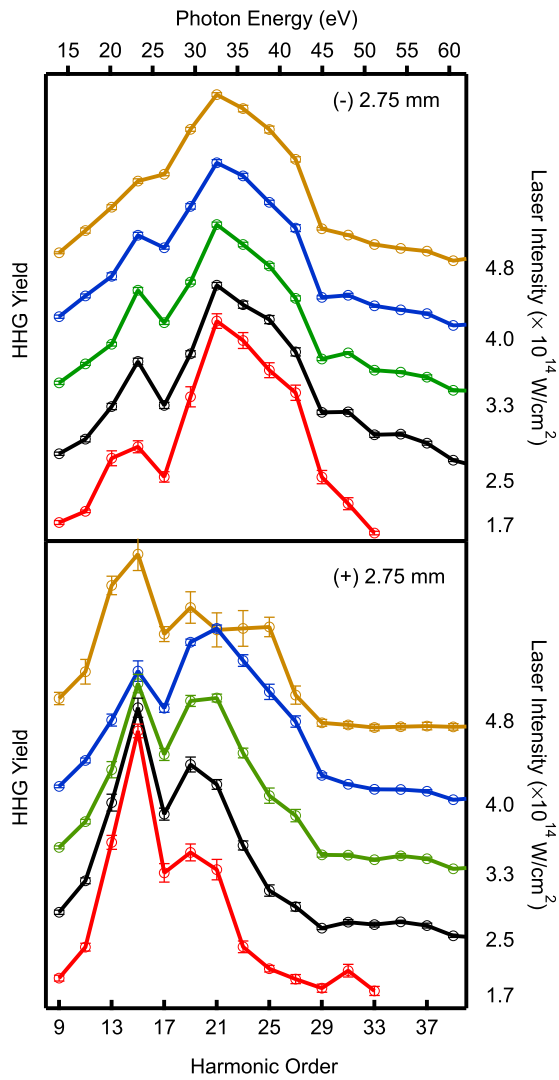

FIG. 3. Intensity dependence of the measured SF_6 harmonic spectrum at (−) and (+) 2.75 mm.

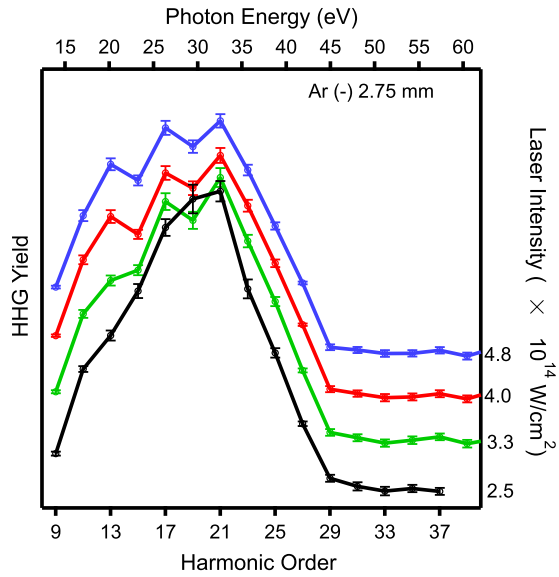

FIG. 4. Intensity dependence of the measured Ar harmonic spectrum at (−) 2.75 mm.

calculations, the scattering basis set was the same as was used to describe the target states, i.e., the 6-311+G(2d) basis set. In these coupled channel calculations, the target states are represented as single configuration state function (CSF) wave functions constructed from the Hartree-Fock orbitals of the initial state, i.e., MCFCHF calculations. These calculations were performed using the D_{2h} point group, which is the largest abelian subgroup of O_h. The channel expansion included the $1t_{1g}$ (HOMO), $5t_{1u}$ (HOMO-1), $1t_{2u}$ (HOMO-2), and $3e_g$ (HOMO-3) ion states, which in D_{2h} symmetry leads to 11 coupled channels. The intra-channel and inter-channel interactions in the calculations included both local static and non-local exchange type interactions consistent with the single CSFs used to represent the ion states. In the computation of the wave packet, we employed a laser pulse (800 nm) with a peak intensity of 1.5×10^{14} W/cm^2.

One element of the QRS theory is the use of the reference atom through $X^{\text{ref}}(\omega)$ defined in Eq. (5). In Fig. 5 we have plotted the $X^{\text{ref}}(\omega)$, computed using the SFA approximation, as a function of energy for the three IPs considered in this study. For the higher IP reference atoms, a considerable amount of structure can be seen when the full integral from Eq. (11) of Ref. 7 is used. If $X^{\text{ref}}(\omega)$ were used without modification, this structure would also be visible in the final computed HHG spectra. We note however, in HHG spectra from single-atom/molecule calculations, even when derived from the solution of the TDSE, there are normally many structures. Much of this structure would be suppressed with the inclusion of macroscopic propagation in the simulation. The reason for this suppression is mostly due to suppression of the long trajectories, whose phases are more sensitive to laser intensity. The structures that survive the macroscopic propagation are typically due to structures in transition dipoles found in the photorecombination step. Unfortunately, macroscopic propagation simulations are very time-consuming. To remove such structure, we have used restricted time limits on the integral for the induced dipoles in the SFA approximation. In Eq. (11) of Ref. 7, we integrate over $\tau = 0 \rightarrow 0.65\,T$ for short trajectories (STs) and over $\tau = 0.65\,T \rightarrow T$ for long trajectories (LTs), where T is the laser period. We also used a Fermi type window function to make the cutoffs at $0.65\,T$ and at T smoother. Contributions from $\tau > T$ would correspond to high-order returns, which contribute mostly to low harmonics, below about $I_i + 1.5\,U_p = 30$ eV in SF_6. At low energies, the computed LT and ST wave packets drop faster than total wave packet with the full integral over τ. However, contributions from high-order returns are suppressed significantly during macroscopic propagation.[55] The value of $0.65\,T$ was chosen so that ST and LT wave packets coincide at the cutoff. To be consistent with the experimental conditions, all subsequent QRS results presented here, based on the SFA approximation for model reference atom, will be for ST calculations.

In Fig. 5, we also show the wave packet generated from the experimental Ar HHG spectrum with the focus at (−) 2.75 mm and an intensity of 2.5×10^{14} W/cm^2 using Eq. (12) and using experimental total and differential photoionization cross sections of Ar.[56,57] We see that the fall-off at high energy in the wave packet generated is pushed to higher energy compared to the SFA results. This is a consequence of the fact that the photoionization differential cross section of Ar, $\sigma_i^{\text{ref}}(\omega)\left[1 + \beta_i^{\text{ref}}(\omega)\right]$, has a deep Cooper minimum at 50 eV which is more pronounced than the minimum seen in the HHG intensity for Ar near that energy. Thus Ar is not a satisfactory reference atom at energies near the Cooper minimum. Nonetheless, below we will consider the use of the Ar wave packet in the simulation of the SF_6 HHG generation from the $1t_{1g}$ (HOMO) orbital.

The two panels in the left column of Fig. 6 show the photoionization cross sections for the first three valence subshells of SF_6 computed using the FCHF (top) and MCFCHF (bottom) approximations.[44] Photoionization in the FCHF approximation from the $1t_{1g}$ subshell has a broad shape resonance spanning from 20 eV to 50 eV of photon energy, which is attributed to $1t_{1g} \rightarrow k\,t_{2u}$ transition. Ionization from the $5t_{1u}$ and $1t_{2u}$ subshells have relatively narrow features at ~24 eV and ~38 eV which are due to shape resonances in the kt_{2g} and ke_g continua.[52] The MCFCHF photoionization cross sections have the same resonant features; however, due to inter-channel coupling, a given resonance in one channel affects the cross sections in the other channels. This is particularly noticeable for the resonances at ~24 eV which leads to a strong feature in the $1t_{1g}$ channels at that energy which is not present in the FCHF calculations. We also note that the position of the resonance features in the MCFCHF photoionization cross sections is consistently shifted up by ~2 eV compared to the experimental positions.[44]

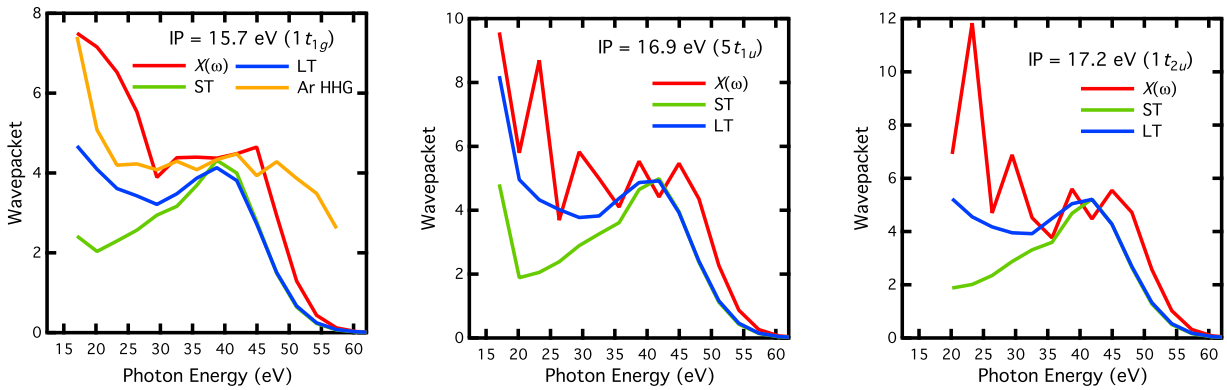

FIG. 5. $X^{\text{ref}}(\omega)$ for short (ST), long (LT), and for the full SFA integration. For HHG generation from the $1t_{1g}$ (HOMO), the wave packet generated from the experimental Ar HHG with the focus at (−) 2.75 mm and an intensity of 2.5×10^{14} W/cm^2 using Eq. (12) is also given.

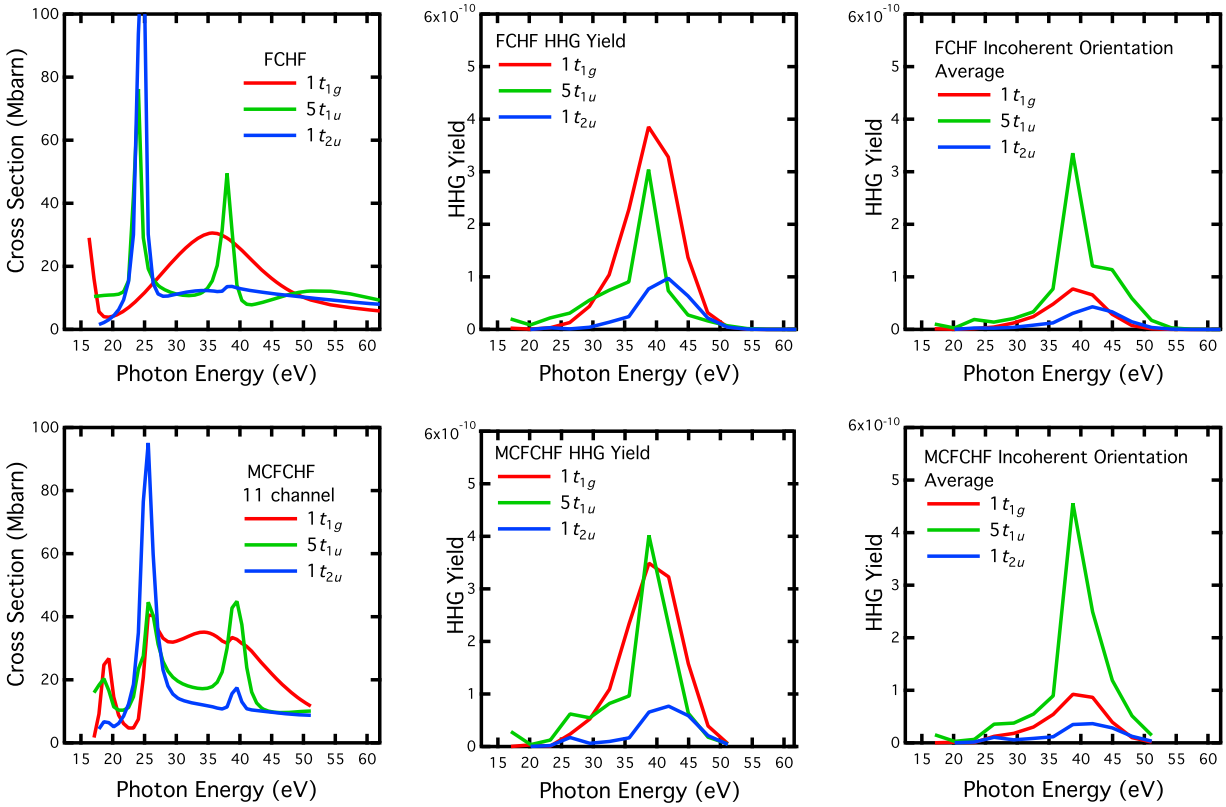

FIG. 6. Photoionization cross sections and QRS HHG spectra of SF_6 for the outer three valence orbitals, $1t_{1g}$ (HOMO), $5t_{1u}$ (HOMO-1), and $1t_{2u}$ (HOMO-2). Left column is the computed photoionization cross sections. Center column is the QRS HHG spectra from the different channel terms in Eq. (8), which has a coherent orientation average. Right column is the approximate separate-channel HHG spectra obtained from incoherent orientation average given in Eq. (9). The top row contains the results for the single-channel FCHF calculations and the bottom row has the corresponding data from the coupled channel MCFCHF calculations.

Using the dipole matrix elements from both the FCHF and MCFCHF photoionization calculations, we then used the QRS theory to compute the HHG spectrum for the $1t_{1g}$ (HOMO), $5t_{1u}$ (HOMO-1), and $1t_{2u}$ (HOMO-2) orbitals. In the middle column of Fig. 6, we show the results for a coherent orientation average but where the different channels are treated separately, this is equivalent to plotting the separate-channel contributions to S' as defined in Eq. (8). The calculated HHG yields from the $1t_{1g}$ and $5t_{1u}$ subshells, in both the FCHF and MCFCHF calculations, exhibit a peak centered near 40 eV (H25). The HHG from the $1t_{1g}$ (HOMO) is strong in this energy region due to the broad kt_{2u} shape resonance present in the $1t_{1g}$ photoionization cross section, as shown in the left column of the figure, whereas the $5t_{1u}$ (HOMO-1) is enhanced by a narrow shape resonance in the ke_g continuum. The computed QRS spectra are on the same scale and are plotted as the power spectrum in atomic units as defined in Eq. (1). Thus, while it is clear that contributions from the $1t_{1g}$ (HOMO) and $5t_{1u}$ (HOMO-1) both make substantial contributions to the harmonic yield at most harmonic orders, the shape resonance from the $5t_{1u}$ and $1t_{2u}$ orbitals at 26 eV (H17) enhances the harmonic yield near these resonances.

We have also computed the separate-channel HHG spectra using the incoherent orientation averages, S'', as given in Eq. (9). The values of $\overline{N}$ obtained from the SFA tunneling rates using Eq. (10) were 6.31×10^{-5} for the $1t_{1g}$ orbital (HOMO), 2.10×10^{-4} for the $5t_{1u}$ orbital (HOMO-1), and 4.35×10^{-5} for the $1t_{2u}$ orbital (HOMO-2), which gives relative orientation averaged tunneling intensities of 0.30:1.0:0.21, which are nearly the same as the relative tunneling rates reported by Ferré *et al.*[31] of 0.35:1:0.22. The separate-channel HHG computed using incoherent orientation averages is reported in the two panels in the right column of Fig. 6. Comparing these results to the QRS HHG in the middle panels, obtained with the correct orientation average, we see that the incoherent orientation average has many of the same features. However the two calculations have dramatically different relative intensities, in particular the $1t_{1g}$ (HOMO) and $5t_{1u}$ (HOMO-1) channels have very similar peak intensities using the coherent orientation average, whereas in the QRS calculation with the incoherent orientation average, the $5t_{1u}$ (HOMO-1) peak is about five times stronger than the peak $1t_{1g}$ (HOMO).

In Fig. 7 we present a comparison of the separate-channel coherent-orientation-averaged QRS results for HHG generated from the $1t_{1g}$ (HOMO) orbital using the SFA wave packet with short trajectories and using the wave packet obtained from the Ar HHG spectrum using Eq. (12). We can see that the two computed spectra are very similar except for energies near 50 eV where the Cooper minimum in the Ar photoionization cross section makes the wave packet obtained from the Ar HHG less reliable.

In Fig. 8 we compare the results of Eqs. (8) and (9) for the total QRS HHG spectrum, which are just the incoherent sum of the separate-channel QRS HHG spectra presented in Fig. 6.

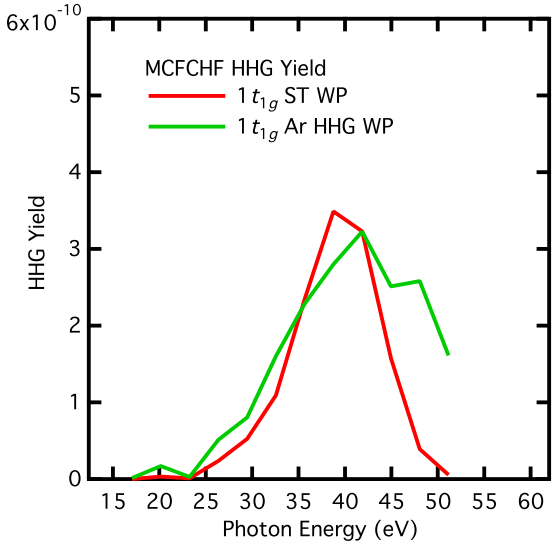

FIG. 7. Comparison of QRS $1t_{1g}$ (HOMO) yield from the short trajectory wave packet calculation and using the experimental wave packet constructed from Ar HHG data using Eq. (12).

We can see that the summed results for the coherent orientation average in the upper panel and the incoherent orientation average shown in the lower panel are very similar, although the relative contributions from the different orbitals are very different for these two cases.

Finally, in Fig. 9, we present the coherent channel sum as given in Eq. (7) for the MCFCHF QRS calculation. We can see that the coherent channel sum leads to an enhancement in the HHG signal with only minor changes in the qualitative features of the spectrum.

V. DISCUSSION

This paper focuses on separating the phase matching effects from the photorecombination dynamics by measuring the effect of changing the phase matching conditions between the laser and the electron wave packet that gives rise to the harmonic signal. Under such conditions, a single molecule model of HHG, such as the QRS, should be close to the experimental HHG spectrum. The previous discussions of macroscopic propagation effects have been restricted to the HHG properties of atomic targets and aligned molecular targets,[58] while previous articles comparing the photorecombination cross section to the ionization cross section have focused on calculations for the wave packet to account for the phase inherent in the HHG signal.[7,59] Extending these calculations to a complex molecule such as SF_6, however, presents serious complications avoided for atomic targets. We hope to clarify phase matching conditions for highly symmetric molecular targets and the robustness of HHG spectroscopy to macroscopic conditions with a focus on the shape resonances present in the photorecombination dynamics of SF_6. The effect of shape resonances on HHG, specifically, has not been determined for larger targets with a complex electronic distribution. Changes in phase matching conditions, particularly in aligned systems, can affect the yield of individual harmonics,[13] complicating the aim of systematically correlating photoionization dynamics

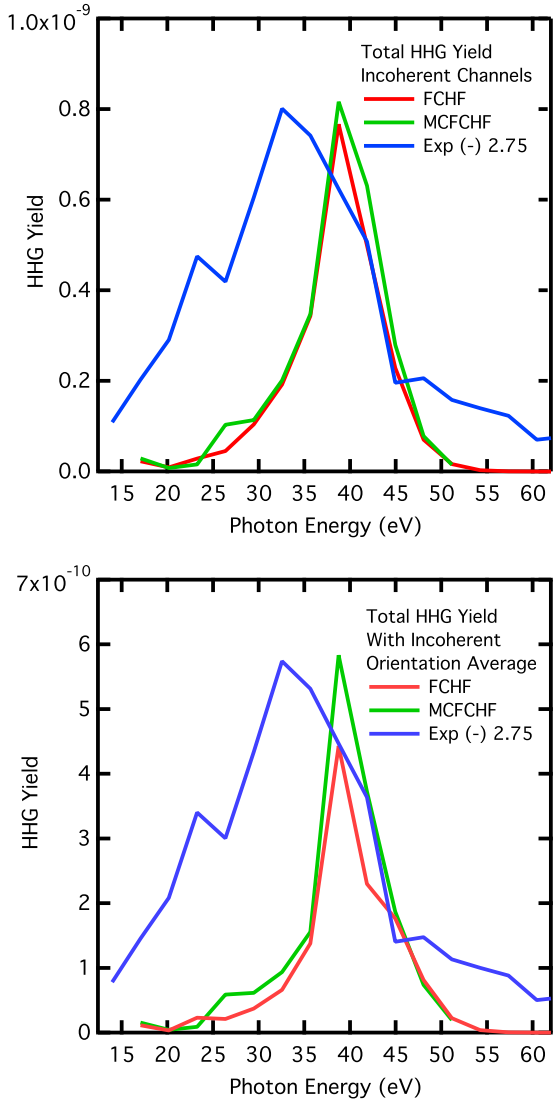

FIG. 8. Top panel: The total of the QRS results from the three outermost valence orbitals of SF_6 shown in the middle column in Fig. 6. Bottom panel: The corresponding total of the incoherent orientation averages shown in the right panel in Fig. 6. The results in both panels are compared to the experimental HHG spectrum at 4.0×10^{14} W/cm^2 with the focal point at (−) 2.75 mm. The experimental scale is arbitrary and selected so that the maximum HHG yield is the same as the MCFCHF QRS results.

and HHG spectra. To quantify an optimal set of phase matching conditions, i.e., experimental parameters at which cross section data are most simply extracted from HHG spectra, we examined the harmonic spectrum as a function of significant changes in both the location of the focal point with respect to the center of the gas jet and the laser intensity. We now compare features in the harmonic spectrum that are independent of change in the phase matching with the calculated results utilizing the QRS method. Such features are strongly influenced by the photorecombination step and thus should be well represented in the QRS.

When the focus is located a few mm in front of the center of the gas jet, i.e., at a "(−)" position, the single atom or molecule harmonic phase is partially cancelled by the Gouy phase near the focus of the laser,[9,60] which in turn flattens the phase of the wave packet, making it less susceptible to changes in the laser intensity.[10] Assuming that the

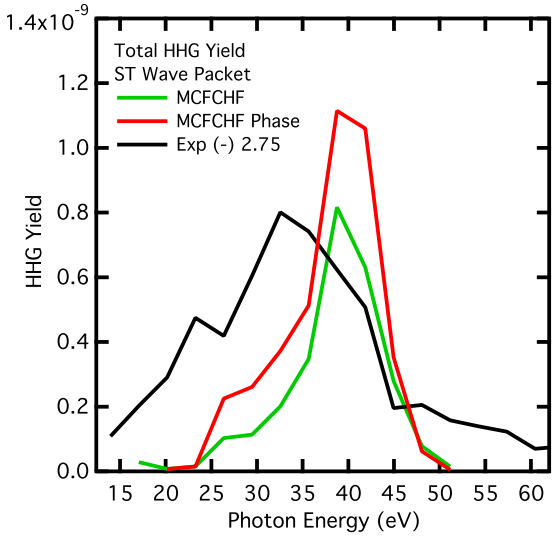

FIG. 9. Comparison of HHG yield computed from the incoherent sum from the different channels using Eq. (8) (green), the coherent sum over the channels with the appropriate phases using Eq. (7) (red), and the experimental results (black) with laser intensity of 4.0×10^{14} W/cm^2 with the focal point at (−) 2.75 mm.

positions of highest phase stability are also the positions where best phase matching occurs, these are the positions at which we conclude the extraction of photorecombination dynamics from the harmonic spectra is the most realistic.[61,62] As such, we use (−) 2.75 mm as the position of note for the remainder of the paper and comparisons to the theoretical models.

The experimental harmonic spectrum of SF_6 at (−) 2.75 mm and 4.0×10^{14} W/cm^2 is presented in Fig. 8 along with the incoherent sum of the QRS results found in Eqs. (8) and (9) of the separate-channel HHG spectra shown in Fig. 6. We see that the QRS HHG signal summed over channels has a strong peak at ∼40 eV, which is narrower than the peak in the experimental spectrum. There is also a shoulder in the MCFCHF spectra at around 27 eV. As observed in the photoionization cross sections, the resonance features in the HHG obtained using the MCFCHF calculation are found to be ∼2 eV higher than the corresponding experimental features.[44]

In our experimental results, there is a peak in the HHG spectrum in the region between 20 and 26 eV (H13–H17). In this energy region, we see that a shape resonance with t_{2g} symmetry influences the $5t_{1u}$ (HOMO-1) and $1t_{2u}$ (HOMO-2) contribution photoionization cross sections. However, in the QRS spectra, the resulting feature is not very strong. To some extent this may be due to the fact that the resonances are very narrow, so that a slight change in the location of the harmonic energies can lead to somewhat different relative prominence of the two resonance features in the predicted QRS spectra. The qualitative agreement between features of the experimental HHG yield and QRS results suggests that the spectrum is mostly a result of HHG by the $1t_{1g}$ (HOMO) and the $5t_{1u}$ (HOMO-1) orbitals. The low energy feature comes from the resonance in the $5t_{1u}$ (HOMO-1) and $1t_{2u}$ (HOMO-2) channels, either directly in the HHG spectrum for those channels or through the interchannel coupling to the $1t_{1g}$ (HOMO) channel in the photorecombination dynamics.

The coherent channel sum of the MCFCHF QRS induced dipoles, shown in Fig. 9, does not change the qualitative interpretation of the observed HHG spectrum, although the quantitative values are changed due the apparent constructive combination of the HHG from the $1t_{1g}$ (HOMO) and $5t_{1u}$ (HOMO-1) channels.

The experimental results presented here are comparable to those published recently,[31,32] but the differing interpretations should be addressed. Specifically, Ferré *et al.* used the measured phase jump around 23 eV (H17) to confirm the influence of a shape resonance from the $5t_{1u}$ (HOMO-1). However, we find that there is insufficient evidence to suggest that the absence of this phase shift at higher energies is indicative of a structureless portion of the harmonic spectrum. It should be noted that a broad peak with a maximum at 29.5 eV (H19) is visible in the experimental HHG spectrum of SF_6 from Ferré *et al.*,[31] similar to our experimental results at (+) 1.7 mm. However, as seen above, the phase matching conditions at this focal point position are expected to strongly enhance the features at low energy relative to what would be found using an isolated molecule theory such as the QRS.[61,62]

The total of the incoherent orientation averages, shown in the lower panel of Fig. 8, has features that are qualitatively similar to those found in the coherent orientation averaged QRS calculations shown in the upper panel. However, the coherent orientation averaged QRS calculation indicates that the $1t_{1g}$ (HOMO) and the $5t_{1u}$ (HOMO-1) HHG make similar contribution to the total spectrum above 26 eV. This is in contrast to the incoherent orientation average which indicates that the $5t_{1u}$ (HOMO-1) HHG is much larger than $1t_{1g}$ (HOMO) over the 17-50 eV energy range considered here. Even though the mean tunneling rates and cross sections are comparable, the coherent orientation averaging suppresses the $5t_{1u}$ (HOMO-1) HHG rate by a factor of ∼5.

The QRS model as applied here has a few significant limitations, which may restrict the accuracy possible for the model. The electronic wave functions used, even in the MCFCHF approximation, neglect correlation effects in the ion target states and have limited dynamic target response in the scattering calculations due to the truncation of the close-coupling expansion. Additionally, the use of the fixed-nuclei approximation implies that we have neglected any nuclear motion that might occur during the HHG process in addition to neglecting the distribution of geometries found in the ground vibrational state of SF_6 which is known to significantly modify the photoionization cross section in the $5t_{1u}$ channel.[51] In the case of SF_6, the fact that all of the orbitals being considered in the HHG process are degenerate, one might expect that symmetry breaking effects such as Jahn-Teller distortions might affect the HHG process.[63,64] Furthermore, we have neglected the coupling between the ion states and the IR field. Note that the energy separation between the HOMO and HOMO-2 is nearly resonant with the IR photon energy and we compute a strong transition moment between those states of 3.7 D. Additional experimental data using different wave lengths would be useful in identifying such effects.[65] Finally we note that with the experimental laser intensity used here, between 1.7

and 5.2×10^{14} W/cm^2, tunneling is the main mechanism for ionization,[66] but multiphoton ionization that is not included in the QRS model also contributes.

VI. CONCLUSIONS

We have measured the HHG spectrum of SF_6 over a broad range of phase matching conditions, identifying those features which are insensitive to those conditions and thus should be well represented in the single molecule QRS model used here to model these spectra. In particular, the features occurring at 23 and 33 eV (H15 and H21) are persistent over a broad range of phase matching conditions and varying laser intensity. A comparison of the experimental and QRS spectra found multiple orbital contributions as well as multiple shape resonance effects in the HHG spectrum of SF_6.

We found that the HHG spectrum predicted with a coherent orientation average was significantly different from that obtained from an incoherent orientation average. Furthermore, the coupled channel computation for the recombination step of the QRS model indicated that the narrow resonance near 23 eV contributed to the overall HHG signal both in the $1t_{1g}$ HOMO channel, through interchannel coupling, and in the $5t_{1u}$ (HOMO-1) and t_{2u} (HOMO-2) channels where the shape resonances occur in single-channel calculations.

Similar to the previous findings of Ferré *et al.*,[31] though by different means, our results strongly indicate that the $5t_{1u}$ subshell (HOMO-1) is responsible for the features in lower order harmonics (H11-H17, 17 eV–26 eV), and a shape resonance arising from this orbital is evident in the harmonic spectrum at 23 eV (H15). Additionally, we find that the spectrum of the higher energy harmonics generated in SF_6 has similar contributions from the $1t_{1g}$ (HOMO) and $5t_{1u}$ (HOMO-1) HHG channels, showing evidence of two shape resonances centered at 33 eV (H21).

ACKNOWLEDGMENTS

Work at Louisiana State University and Texas A&M University was supported by the United States Department of Energy (DOE), Office of Science, Basic Energy Science (BES), Geoscience, and Biological Divisions, under Award No. DE-SC0012198. Work at Kansas State University was supported by DOE, Office of Science, BES, Geoscience, and Biological Divisions, under Award No. DE-FG02-86ER13491. J.J. was partially supported by the Robert A. Welch Foundation (Houston, Texas) under Grant No. A-1020. Also, the assistance and computer time provided by the Supercomputing Facility at Texas A&M University are acknowledged.

[1] K. J. Schafer, B. Yang, L. F. DiMauro, and K. C. Kulander, Phys. Rev. Lett. **70**, 1599 (1993).
[2] P. B. Corkum, Phys. Rev. Lett. **71**, 1994 (1993).
[3] T. Popmintchev, M.-C. Chen, A. Bahabad, M. Gerrity, P. Sidorenko, O. Cohen, I. P. Christov, M. M. Murnane, and H. C. Kapteyn, Proc. Natl. Acad. Sci. U. S. A. **106**, 10516 (2009).
[4] M. Hentschel, R. Kienberger, C. Spielmann, G. A. Reider, N. Milosevic, T. Brabec, P. Corkum, U. Heinzmann, M. Drescher, and F. Krausz, Nature **414**, 509 (2001).
[5] F. Krausz and M. Ivanov, Rev. Mod. Phys. **81**, 163 (2009).
[6] H. Kapteyn, O. Cohen, I. Christov, and M. Murnane, Science **317**, 775 (2007).
[7] A.-T. Le, R. R. Lucchese, S. Tonzani, T. Morishita, and C. D. Lin, Phys. Rev. A: At., Mol., Opt. Phys. **80**, 013401 (2009).
[8] A.-T. Le, R. R. Lucchese, and C. D. Lin, Phys. Rev. A: At., Mol., Opt. Phys. **87**, 063406 (2013).
[9] M. V. Frolov, N. L. Manakov, T. S. Sarantseva, M. Y. Emelin, M. Y. Ryabikin, and A. F. Starace, Phys. Rev. Lett. **102**, 243901 (2009).
[10] H. J. Wörner, H. Niikura, J. B. Bertrand, P. B. Corkum, and D. M. Villeneuve, Phys. Rev. Lett. **102**, 103901 (2009).
[11] X. Ren, V. Makhija, A.-T. Le, J. Troß, S. Mondal, C. Jin, V. Kumarappan, and C. Trallero-Herrero, Phys. Rev. A: At., Mol., Opt. Phys. **88**, 043421 (2013).
[12] A. D. Shiner, B. E. Schmidt, C. Trallero-Herrero, H. J. Worner, S. Patchkovskii, P. B. Corkum, J.-C. Kieffer, F. Legare, and D. M. Villeneuve, Nat. Phys. **7**, 464 (2011).
[13] B. A. Sickmiller and R. R. Jones, Phys. Rev. A: At., Mol., Opt. Phys. **80**, 031802 (2009).
[14] C. Winterfeldt, C. Spielmann, and G. Gerber, Rev. Mod. Phys. **80**, 117 (2008).
[15] M. B. Gaarde, F. Salin, E. Constant, P. Balcou, K. J. Schafer, K. C. Kulander, and A. L'Huillier, Phys. Rev. A: At., Mol., Opt. Phys. **59**, 1367 (1999).
[16] C. Jin, J. B. Bertrand, R. R. Lucchese, H. J. Worner, P. B. Corkum, D. M. Villeneuve, A. T. Le, and C. D. Lin, Phys. Rev. A: At., Mol., Opt. Phys. **85**, 013405 (2012).
[17] M. Tudorovskaya and M. Lein, Phys. Rev. A: At., Mol., Opt. Phys. **84**, 013430 (2011).
[18] C. D. Lin, A.-T. Le, Z. Chen, T. Morishita, and R. Lucchese, J. Phys. B: At. Molec. Opt. Phys. **43**, 122001 (2010).
[19] J. P. Farrell, L. S. Spector, B. K. McFarland, P. H. Bucksbaum, M. Guhr, M. B. Gaarde, and K. J. Schafer, Phys. Rev. A: At., Mol., Opt. Phys. **83**, 023420 (2011).
[20] J. B. Bertrand, H. J. Worner, P. Hockett, D. M. Villeneuve, and P. B. Corkum, Phys. Rev. Lett. **109**, 143001 (2012).
[21] M. C. H. Wong, A. T. Le, A. F. Alharbi, A. E. Boguslavskiy, R. R. Lucchese, J. P. Brichta, C. D. Lin, and V. R. Bhardwaj, Phys. Rev. Lett. **110**, 033006 (2013).
[22] T. Gustafsson, Phys. Rev. A: At., Mol., Opt. Phys. **18**, 1481 (1978).
[23] J. L. Dehmer, A. C. Parr, S. Wallace, and D. Dill, Phys. Rev. A: At., Mol., Opt. Phys. **26**, 3283 (1982).
[24] B. M. Addison-Jones, K. H. Tan, B. W. Yates, J. N. Cutler, G. M. Bancroft, and J. S. Tse, J. Electron Spectrosc. Relat. Phenom. **48**, 155 (1989).
[25] D. M. P. Holland, M. A. MacDonald, P. Baltzer, L. Karlsson, M. Lundqvist, B. Wannberg, and W. v. Niessen, Chem. Phys. **192**, 333 (1995).
[26] A. J. Yencha, D. B. Thompson, A. J. Cormack, D. R. Cooper, M. Zubek, P. Bolognesi, and G. C. King, Chem. Phys. **216**, 227 (1997).
[27] L. Yang, H. Agrena, V. Carravettab, O. Vahtras, L. Karlsson, B. Wannberg, D. M. P. Holland, and M. A. MacDonald, J. Electron Spectrosc. Relat. Phenom. **94**, 163 (1998).
[28] A. P. P. Natalense and R. R. Lucchese, J. Chem. Phys. **111**, 5344 (1999).
[29] M. Stener, D. Toffoli, G. Fronzoni, and P. Decleva, J. Chem. Phys. **124**, 114306 (2006).
[30] A. Rupenyan, P. M. Kraus, J. Schneider, and H. J. Wörner, Phys. Rev. A: At., Mol., Opt. Phys. **87**, 033409 (2013).
[31] A. Ferré, A. E. Boguslavskiy, M. Dagan, V. Blanchet, B. D. Bruner, F. Burgy, A. Camper, D. Descamps, B. Fabre, N. Fedorov, J. Gaudin, G. Geoffroy, J. Mikosch, S. Patchkovskii, S. Petit, T. Ruchon, H. Soifer, D. Staedter, I. Wilkinson, A. Stolow, N. Dudovich, and Y. Mairesse, Nat. Commun. **6**, 5952 (2015).
[32] B. Manschwetus, N. Lin, J. Rothhardt, R. Guichard, T. Auguste, A. Camper, P. Breger, J. Caillat, M. Geleoc, T. Ruchon, R. Taieb, B. Carre, and P. Salieres, J. Phys. Chem. A **119**, 6111 (2015).
[33] B. Langdon, J. Garlick, X. Ren, D. J. Wilson, A. M. Summers, S. Zigo, M. F. Kling, S. Lei, C. G. Elles, E. Wells, E. D. Poliakoff, K. D. Carnes, V. Kumarappan, I. Ben-Itzhak, and C. A. Trallero-Herrero, Opt. Express **23**, 4563 (2015).
[34] D. Telnov and S.-I. Chu, Phys. Rev. A: At., Mol., Opt. Phys. **76**, 043412 (2007).
[35] M. Lewenstein, P. Balcou, M. Y. Ivanov, A. L'Huillier, and P. B. Corkum, Phys. Rev. A: At., Mol., Opt. Phys. **49**, 2117 (1994).
[36] C. B. Madsen and L. B. Madsen, Phys. Rev. A: At., Mol., Opt. Phys. **76**, 043419 (2007).
[37] S. Minemoto, T. Umegaki, Y. Oguchi, T. Morishita, A.-T. Le, S. Watanabe, and H. Sakai, Phys. Rev. A: At., Mol., Opt. Phys. **78**, 061402 (2008).
[38] T. Morishita, A. T. Le, Z. Chen, and C. D. Lin, Phys. Rev. Lett. **100**, 013903 (2008).

[39]R. R. Lucchese, G. Raseev, and V. McKoy, Phys. Rev. A: At., Mol., Opt. Phys. **25**, 2572 (1982).
[40]F. A. Gianturco, R. R. Lucchese, and N. Sanna, J. Chem. Phys. **100**, 6464 (1994).
[41]B. Basden and R. R. Lucchese, Phys. Rev. A: At., Mol., Opt. Phys. **37**, 89 (1988).
[42]T. N. Rescigno, B. H. Lengsfield III, and C. W. McCurdy, in *Modern Electronic Structure Theory*, edited by D. R. Yarkony (World Scientific, Singapore, 1995), Vol. 1, p. 501.
[43]T. Rescigno and A. Orel, Phys. Rev. A: At., Mol., Opt. Phys. **43**, 1625 (1991).
[44]J. Jose, R. R. Lucchese, and T. N. Rescigno, J. Chem. Phys. **140**, 204305 (2014).
[45]M. B. Gaarde, J. L. Tate, and K. J. Shafer, J. Phys. B: At., Mol. Opt. Phys. **41**, 132001 (2008).
[46]S. Haessler, J. Caillat, and P. Salieres, J. Phys. B: At., Mol. Opt. Phys. **44**, 203001 (2011).
[47]P. Salieres, A. L'Huillier, and M. Lewenstein, Phys. Rev. Lett. **74**, 3776 (1995).
[48]S. Baker, J. S. Robinson, C. A. Haworth, H. Teng, R. A. Smith, C. C. Chirila, M. Lein, J. W. G. Tisch, and J. P. Marangos, Science **312**, 424 (2006).
[49]M. Bellini, C. Lyngå, A. Tozzi, M. B. Gaarde, T. W. Hänsch, A. L'Huillier, and C. G. Wahlström, Phys. Rev. Lett. **81**, 297 (1998).
[50]J. Higuet, H. Ruf, N. Thiré, R. Cireasa, E. Constant, E. Cormier, D. Descamps, E. Mével, S. Petit, B. Pons, Y. Mairesse, and B. Fabre, Phys. Rev. A: At., Mol., Opt. Phys. **83**, 053401 (2011).
[51]J. Jose and R. R. Lucchese, Chem. Phys. **447**, 64 (2015).
[52]R. R. Lucchese and F. A. Gianturco, Int. Rev. Phys. Chem. **15**, 429 (1996).
[53]M. J. Frisch, G. N. Trueks, and H. B. Schlegel, GAUSSIAN 03, Revision C.02, Gaussian, Inc., Wallingford, CT, 2004.
[54]*Structure of Free Polyatomic Molecules, Basic Data*, edited by K. Kuchitsu (Springer, Berlin, 1998).
[55]A. T. Le, H. Wei, C. Jin, V. N. Tuoc, T. Morishita, and C. D. Lin, Phys. Rev. Lett. **113**, 033001 (2014).
[56]J. A. R. Samson and W. C. Stolte, J. Electron Spectrosc. Relat. Phenom. **123**, 265 (2002).
[57]R. G. Houlgate, J. B. West, K. Codling, and G. V. Marr, J. Electron Spectrosc. Relat. Phenom. **9**, 205 (1976).
[58]C. Trallero-Herrero, J. Cheng, B. E. Schmidt, A. D. Shiner, J. C. Kieffer, P. B. Corkum, D. M. Villeneuve, C. D. Lin, F. Légaré, and A. T. Le, J. Phys. B: At., Mol. Opt. Phys. **45**, 011001 (2012).
[59]A.-T. Le, R. R. Lucchese, and C. D. Lin, Phys. Rev. A: At., Mol., Opt. Phys. **88**, 021402 (2013).
[60]A. Rupenyan, J. B. Bertrand, D. M. Villeneuve, and H. J. Wörner, Phys. Rev. Lett. **108**, 033903 (2012).
[61]C. Jin, H. J. Wörner, V. Tosa, A.-T. Le, J. B. Bertrand, R. R. Lucchese, P. B. Corkum, D. M. Villeneuve, and C. D. Lin, J. Phys. B: At., Mol. Opt. Phys. **44**, 095601 (2011).
[62]C. Jin, A.-T. Le, and C. D. Lin, Phys. Rev. A: At., Mol., Opt. Phys. **83**, 023411 (2011).
[63]N. L. Wagner, A. Wuest, I. P. Christov, T. Popmintchev, X. Zhou, M. M. Murnane, and H. C. Kapteyn, Proc. Natl. Acad. Sci. U. S. A. **103**, 13279 (2006).
[64]Z. B. Walters, S. Tonzani, and C. H. Greene, J. Phys. B: At., Mol. Opt. Phys. **40**, F277 (2007).
[65]P. M. Kraus, B. Mignolet, D. Baykusheva, A. Rupenyan, L. Horný, E. F. Penka, G. Grassi, O. I. Tolstikhin, J. Schneider, F. Jensen, L. B. Madsen, A. D. Bandrauk, F. Remacle, and H. J. Wörner, Science **350**, 790 (2015).
[66]L. V. Keldysh, Sov. Phys. - JETP **20**, 1307 (1965).